

Supplemental Information Appendix

Atmospheric autoxidation is increasingly important in urban and suburban North America

Eric Praske^a, Rasmus V. Otkjær^b, John D. Crouse^c, J. Caleb Hethcox^a, Brian M. Stoltz^a, Henrik

G. Kjaergaard^{b}, Paul O. Wennberg^{c,d*}*

^a Division of Chemistry and Chemical Engineering, California Institute of Technology, 1200 E. California Blvd, Pasadena, CA 91125

^b Department of Chemistry, University of Copenhagen, Universitetsparken 5, DK-2100 Copenhagen Ø, Denmark

^c Division of Geological and Planetary Sciences, California Institute of Technology, 1200 E. California Blvd, Pasadena, CA 91125

^d Division of Engineering and Applied Science, California Institute of Technology, 1200 E. California Blvd, Pasadena, CA 91125

*Correspondence to P.O. Wennberg (wennberg@caltech.edu) and H.G. Kjaergaard (hgk@chem.ku.dk)

Contents

Experimental methods	3
Chemicals and synthesis	3
Chamber and instruments	4
Calculation of bimolecular RO ₂ lifetime	6
Instrumental calibration	8
Structural assignment of the RONO ₂	12
Product yields and branching ratios	14
Uncertainty	16
Computational methods	20
Expression of the rate coefficients	21
Uncertainty	22
High temperature data	25
Deuterated 2-hexanol	26
Diastereomer effects	28
Best fits	31
Previous determination of the 1,6 H-shift	34
Calculations for the hexoxy method	35
Quantification of the 2,5 ketohydroperoxide	38

Experimental methods

We performed a series of oxidation experiments of 2-hexanol with varying NO and HO₂ mixing ratios (and thus varying $\tau_{\text{bimolecular}}$). Gas chromatography coupled with CF₃O⁻ CIMS was used to quantify the relative abundance of the individual RONO₂ isomers formed in these experiments.

Experiments began by adding reagents to a ~1 m³ Teflon bag. A 500 cm³ glass bulb with 2-hexanol vapor was prepared, which underwent serial dilution to achieve the desired mixing ratio and was backfilled with N₂. A separate bulb was similarly prepared containing CH₃ONO. FTIR (Nicolet 560 Magna IR) was used to quantify both gas mixtures using published cross sections (1). Addition of nitric oxide was necessary for certain experiments. For experiments without NO added to the chamber, [NO]₀ was less than 30 pptv in the zero air used to fill the chamber.

Following the collection of background signals in the CIMS instrument, the chamber was illuminated typically for 10-60 minutes depending on experimental conditions. For experiments with $\tau_{\text{bimolecular}} > 30$ s, however, longer oxidation periods ranging 12-16 hours were required to accumulate sufficient products for quantification while simultaneously ensuring that RO₂ self-reactions remained negligible.

Chemicals and synthesis

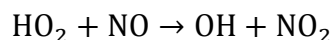
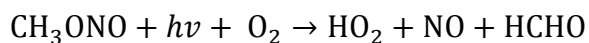
2-hexanol (99%, Sigma-Aldrich), nitric oxide (1993 ± 20 ppmv NO in N₂, Matheson), isopropanol (≥ 99%, Macron), 2-hexanone (Sigma-Aldrich, 98%), and lithium aluminum deuteride (Strem, 98%) were used as purchased. Deuterated 2-hexanol was afforded in 89% yield upon treatment of 2-hexanone (0.500 g, 4.99 mmol) with lithium aluminum deuteride (0.230 g,

5.49 mmol) in THF (16 mL) as described elsewhere (2). Methyl nitrite was synthesized using a method similar to that described in Taylor et al. (3).

A synthetic sample of the 2,5 RONO₂ needed for chromatographic assignment was prepared from the addition of nitric acid to 2,5-dimethyltetrahydrofuran (2,5-diMeTHF, Santa Cruz Biotechnology) as detailed in earlier work (4). Briefly, ~5 mmol of 2,5-diMeTHF was dissolved in DCM, with the reaction vessel submerged in an ice bath, and concentrated HNO₃ was added in a 1.1:1 (HNO₃:2,5-diMeTHF) molar ratio. The vessel was removed from the ice bath and left to stir for 1 hour. The solvent was then removed by boiling under reduced pressure at 23 K.

Chamber and instruments

The chamber configuration and the Gas Chromatograph Chemical Ionization Mass Spectrometer (GC-CIMS) have been documented extensively (5-11). The chamber consists of a ~1 m³ fluorinated ethylene propylene copolymer bag (Teflon-FEP, DuPont) connected to instrumentation by 6.35 mm OD PFA tubing. The chamber is housed inside an enclosure with UV reflective metal flashing. All experiments were conducted at ambient pressure (~745 torr) and at either 296 ± 2 K or 318 ± 5 K. The enclosure is equipped with 8 individually controlled UV blacklights (Sylvania 350). For some experiments, only one bulb was used and a front panel blocked direct illumination such that only the reflection illuminated the chamber. The placement of a back panel (a very poor UV reflector) in addition to the front panel enabled a further reduction of the light flux in some experiments. Modulating the light enabled control over the photolysis of methyl nitrite, used as an oxidant source according to the following reactions:



GC-CIMS, using CF_3O^- reagent ion ($m/z = 85$), was used to quantify multifunctional oxidation products with a detection limit of ~ 10 pptv with a 1 s integration period. The reagent ion was formed by passing 1 ppm CF_3OOCF_3 in N_2 through a radioactive ^{210}Po source. After dilution of the sample flow with N_2 , gas analytes interact with CF_3O^- at a pressure of 35 mbar, forming charged clusters. In order to compensate for variation in the total ion signal, analyte signals were normalized to the sum of the isotope of the reagent ion, $^{13}\text{CF}_3\text{O}^-$, and its clusters with water and H_2O_2 (m/z 104 and m/z 120, respectively). CIMS signal backgrounds were determined prior to initiating photooxidation.

To enable separation of isobaric species, gas chromatography coupled with CF_3O^- CIMS was conducted following oxidation (5, 6, 9, 11-14). Analytes were collected on the head of a 4 m Restek RTX-1701 column using a -10 °C isopropanol bath. The collection temperature could not be significantly reduced without also trapping large quantities of water, which degrades the analysis. After trapping, elution was enabled using a flow of 8 sccm N_2 and a temperature ramping program (30 °C for 0.1 min, $+3$ °C/min until 60 °C, and $+10$ °C/min to 130 °C). The effluent of the column was further diluted with N_2 and transmitted into the CIMS ion-molecule reaction region. Chromatograms of chamber air were collected both before and after the oxidation period.

The concentration of NO present at the beginning of the high-NO experiments was quantified using a 200EU Teledyne-API chemiluminescence NO_x analyzer. Calibration was performed by sampling a 939 ppbv NO standard (Scott-Marrin, Inc.). For those experiments performed without addition of NO, we quantify the NO abundance as described below in the calculation of bimolecular lifetime. A gas chromatograph equipped with a flame ionization

detector (GC-FID, Hewlett Packard 5890 series II Plus) was used to monitor 2-hexanol and the principal oxidation product, 2-hexanone.

Calculation of bimolecular RO₂ lifetime

For the conditions of our experiments, self-reaction of the peroxy radicals is much slower than reaction with either NO or HO₂. Thus, the bimolecular peroxy radical lifetime is given by:

$$\tau_{\text{bimolecular}} = \frac{1}{k_{\text{RO}_2+\text{NO}}[\text{NO}] + k_{\text{RO}_2+\text{HO}_2}[\text{HO}_2]}$$

For experiments where NO is not quantifiable using the chemilluminescence instrument (those without NO added), the bimolecular RO₂ lifetime is estimated using the method described in Crouse et al. (15) and Teng et al. (12). Briefly, we use the observed production rates and yields of hydrogen peroxide, RONO₂, and ROOH together with the recommended rate coefficients for RO₂ + HO₂ ($1.8 \times 10^{-11} \text{ cm}^3 \text{ molec}^{-1} \text{ s}^{-1}$ at 296 K; $1.3 \times 10^{-11} \text{ cm}^3 \text{ molec}^{-1} \text{ s}^{-1}$ at 318 K), and RO₂ + NO ($8.6 \times 10^{-12} \text{ cm}^3 \text{ molec}^{-1} \text{ s}^{-1}$ at 296 K; $7.9 \times 10^{-12} \text{ cm}^3 \text{ molec}^{-1} \text{ s}^{-1}$ at 318 K) (16). The mixing ratio of HO₂ is estimated from the production rate of H₂O₂ (P_{H₂O₂}) and the recommended rate coefficient for the self-reaction of HO₂ (k_{HO₂+HO₂}) including a dependence on water vapor (17):

$$P_{\text{H}_2\text{O}_2} = k_{\text{HO}_2+\text{HO}_2} \times [\text{HO}_2]^2$$

$$k_{\text{HO}_2+\text{HO}_2} = \left(2.2 \times 10^{-13} \exp\left(\frac{600}{T}\right) + 1.9 \times 10^{-33} [\text{M}] \exp\left(\frac{980}{T}\right) \right)$$

$$\times \left(1 + 1.4 \times 10^{-21} [\text{H}_2\text{O}] \exp\left(\frac{2200}{T}\right) \right)$$

$$[\text{HO}_2] = \sqrt{\frac{P_{\text{H}_2\text{O}_2}}{k_{\text{HO}_2+\text{HO}_2}}}$$

Finally, [NO] was inferred based on known [HO₂] and the observed production rates of the hydroxynitrates and peroxides, P_{RONO₂} and P_{ROOH}, respectively:

$$P_{\text{RONO}_2} = \text{BR}_{\text{RONO}_2} \times k_{\text{RO}_2+\text{NO}} \times [\text{NO}] \times [\text{RO}_2]$$

$$P_{\text{ROOH}} = Y_{\text{ROOH}} \times k_{\text{RO}_2+\text{HO}_2} \times [\text{HO}_2] \times [\text{RO}_2]$$

$$[\text{NO}] = \frac{P_{\text{RONO}_2}}{P_{\text{ROOH}}} \frac{Y_{\text{ROOH}}}{\text{BR}_{\text{RONO}_2}} \frac{k_{\text{RO}_2+\text{HO}_2}}{k_{\text{RO}_2+\text{NO}}} [\text{HO}_2]$$

We assume that the yield of the hydroperoxide, Y_{ROOH}, is 1.0 while the nitrate branching ratio (BR_{RONO₂}) is measured as described below. We also account for wall losses of these compounds.

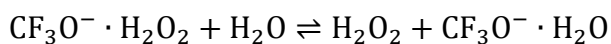
Instrumental calibration

Most of the multifunctional species discussed in this work are not commercially available in pure form. For these species, direct calibration is not possible and an alternative method for the estimation of instrumental sensitivities is required for quantification. We estimate these sensitivities through the calculation of the ion-molecule collision rate coefficients using the parameterization of Su et al. (18), assuming that all collisions lead to formation of quantifiable product ions. We calculate the dipole moments and polarizabilities of closed-shell products arising from the 2,5 RO₂, in addition to all isomers of the 3 major RONO₂, using DFT (B3LYP/6-31+G(d)). Due to the dependence of the dipole moment on structural conformation, we use a weighted average of the located conformers. In contrast, the polarizability does not exhibit a large conformational dependence and the determination was based on the lowest energy conformer. A detailed description of this method is available (19). These properties for species derived from the 2-hexanol system are given in Table S1.

In our estimation of [NO] (see above), we use a ratio of production rates ($\frac{P_{\text{RONO}_2}}{P_{\text{ROOH}}}$), and therefore this expression is only sensitive to the relative calibration factors of these species. Because the calibration factor was only calculated for the 2,5 ROOH isomer, we use the ratio of the RONO₂ and ROOH sensitivities for this isomer. For the determination of the nitrate branching ratios, however, the isomer-specific calibration factors were used. In the case of differing sensitivity for a diastereomeric pair, the average was used.

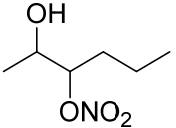
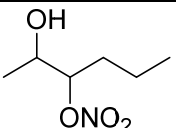
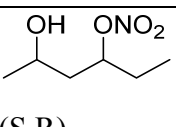
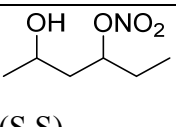
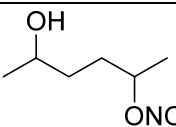
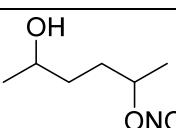
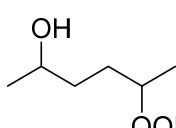
As discussed above, the production rate of H₂O₂ is used to estimate [HO₂] and thereby $\tau_{\text{bimolecular}}$. The efficiency of CF₃O⁻ clustering with H₂O₂ is affected by water vapor according to competing effects: 1) CF₃O⁻•H₂O reacts more efficiently by ligand exchange with H₂O₂ to

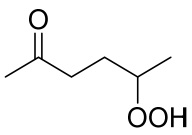
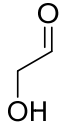
form $\text{CF}_3\text{O}^- \cdot \text{H}_2\text{O}_2$ compared to the CF_3O^- ion and 2) $\text{CF}_3\text{O}^- \cdot \text{H}_2\text{O}_2$ likewise undergoes ligand exchange with water vapor:



In order to account for the changing sensitivity, a calibration for H_2O_2 across a span of water vapor mixing ratios relevant to our experiments was performed. A measured quantity of dilute H_2O_2 was evaporated into our chamber and a small $\sim 0.2 \text{ m}^3$ Teflon bag was prepared with $\sim 1\%$ water vapor in N_2 . The small bag was connected through a critical orifice to the flow tube and a flow controller regulated a quantity of dry N_2 . At the highest setting, dry N_2 overflowed the critical orifice and backflowed into the pillow bag such that no water vapor from the pillow bag was sampled. As the flow rate of N_2 was decreased, however, a mixture of dry N_2 and water vapor entered the flow tube which allowed us to vary the water vapor mixing ratio in the ion region. As discussed by Crouse et al. (6), the instrumental sensitivity toward H_2O_2 increased by 25% over the range of water vapor (30-300 ppm) observed in the 2-hexanol experiments.

Table S1. Calculated average dipole moments ($\bar{\mu}$) and polarizabilities (α) used to determine ion-molecule collision rate coefficients and instrumental sensitivity. k_x is the conformer weighted average collision rate coefficient. The instrumental sensitivity is derived from the ratio of this rate coefficient for each analyte against that of glycolaldehyde ($k = 2.0 \times 10^{-9} \text{ cm}^3 \text{ molecule}^{-1} \text{ s}^{-1}$), for which an experimental determination has been made. Dipole moments and polarizabilities are calculated at the B3LYP/6-31+G(d) level of theory.

molecule	m/z	$\bar{\mu}$ (D)	α (\AA^3)	k_x ($10^{-9} \text{ cm}^3 \text{ molecule}^{-1} \text{ s}^{-1}$)	calculated sensitivity ($\times 10^{-4}$) ^a	experimental sensitivity ($\times 10^{-4}$) ^a
 (S,R)	248	3.2	15	2.4	1.8	-
 (S,S)	248	3.2	15	2.4	1.8	-
 (S,R)	248	4.1	15	2.9	2.2	-
 (S,S)	248	3.8	15	2.7	2.0	-
 (S,R)	248	4.1	15	2.9	2.2	-
 (S,S)	248	4.1	15	2.9	2.2	-
 (S,R) ^b	219	3.8	13	2.8	2.1	-

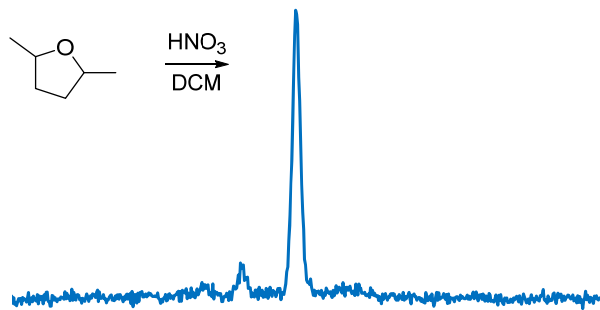
molecule	m/z	$\bar{\mu}$ (D)	α (\AA^3)	k_x ($10^{-9} \text{ cm}^3 \text{ molecule}^{-1} \text{ s}^{-1}$)	calculated sensitivity ($\times 10^{-4}$) ^a	experimental sensitivity ($\times 10^{-4}$) ^a
	217	4.8	12	3.3	2.5	-
	145	2.3	4.5	2.0	-	1.5

^a CF_3O^- CIMS sensitivity (ncts. pptv^{-1}), where ncts. includes normalization to $^{13}\text{CF}_3\text{O}^-$ and its clusters with water and H_2O_2 m/z 86 + m/z 104 + m/z 120

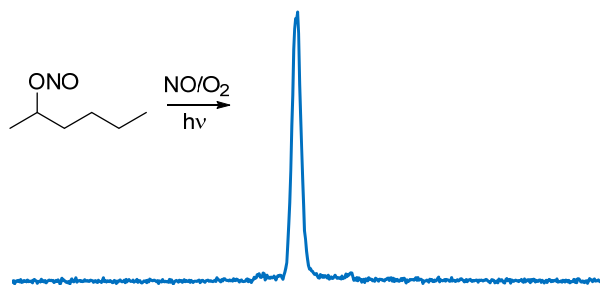
^b The dipole moment and polarizability were only calculated for the S,R diastereomer

Structural assignment of the RONO₂

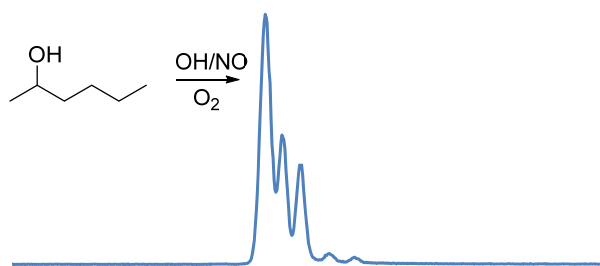
A)



B)



C)



D)

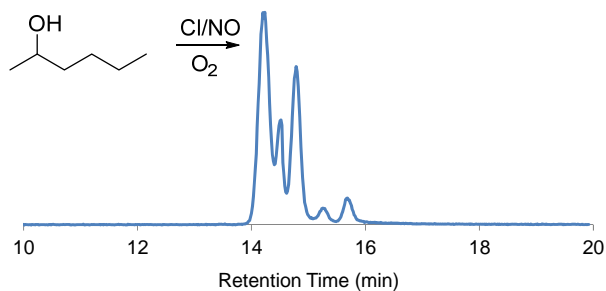


Figure S1. Structural assignment of RONO₂ was performed by chromatographic analysis. Panel A demonstrates GC-CIMS sampling of the dried product mixture following the condensed phase synthesis of 2,5 RONO₂ (see text). All gas-phase photooxidation reactions (panels B-D) were performed under conditions of high NO ([NO]₀ > 350 ppbv), effectively eliminating contribution from unimolecular channels. The corresponding oxidation reactions are indicated. Note that retention times differ from chromatograms shown in the main article and elsewhere in the SI due to slight differences in the instrumental configuration.

The identities of the RONO₂ isomers were assigned following the collection of several chromatograms (see Figure S1). Among the three major peroxy radicals, the OH hydrogen abstraction preference from 2-hexanol as determined by SAR (~0.6, ~0.2, ~0.2 for β, γ, and δ abstraction, respectively) nominally agrees with the isomer distribution observed here (0.66 ± 0.20, 0.17 ± 0.06, 0.17 ± 0.06 at 296 K) (20, 21).

For the 2,5 RONO₂, a synthetic standard was synthesized as described above. The elution time of this peak was found to match that of the major product of 2-hexylnitrite photolysis. Thus, this isomer was conclusively identified. Additional assignments were made by performing oxidation of the alcohol initiated by Cl, exploiting distinct abstraction differences as compared with OH. According to SAR, while C-H bonds that are α and β to a hydroxy group are activated (20, 21), the extent of the activation at more distant sites (γ, δ, ...) is negligible. Abstraction at deactivated sites is enhanced by Cl compared to OH due to distinct activation barriers, producing substantially different chromatographic peak ratios (22, 23). As seen in Figure S1, this effect is most pronounced for the RONO₂ at the 5- and 6-carbon positions (3rd and 5th peaks, respectively, see Figure 1 of the main article for assignment).

Product yields and branching ratios

Table S2. Measured production of RONO₂ following OH reaction of 2-hexanol with [NO]₀ > 350 ppbv. Mixing ratios are expressed in ppbv. ΔRONO₂ represents the sum of all isomers detected during CIMS sampling using a weighted average of the calibration factors for the 3 dominant isomers. The individual isomer yields were calculated by dividing ΔRONO₂ by the GC fractional abundances assuming equal transmission of the isomers. The primary RONO₂ (2,1 and 2,6 RO₂; not shown in the table) were produced in ~5% and ~8% yields at 296 K and 313 K, respectively.

T (K)	ΔRONO ₂	Δ _{2,3} RONO ₂	Δ _{2,4} RONO ₂	Δ _{2,5} RONO ₂	Δ2-hexanol	BR _{RONO₂}
296 ± 2	1.7 ± 0.5	1.1 ± 0.4	0.27 ± 0.09	0.27 ± 0.09	17 ± 0.87	0.25 ± 0.10
313 ± 3	1.3 ± 0.4	0.72 ± 0.3	0.23 ± 0.08	0.25 ± 0.09	19 ± 1.9	0.17 ± 0.07

Experiments performed at [NO]₀ > 350 ppbv enable measurement of the branching ratios of hydroxy nitrates (BR_{RONO₂}) and 2-hexanone, the expected major product following α-OH abstraction in 2-hexanol.

We measured RONO₂ using CIMS, and accounted for a first-order wall loss coefficient of $\sim 8 \times 10^{-6} \text{ s}^{-1}$. A weighted average of the available calibration factors was used to determine ΔRONO₂. The abundance of the minor, primary RONO₂ was estimated using the same average calibration factor as the dipole moments and polarizabilities were not calculated for these isomers. GC-FID was used to quantify both the loss of alcohol (Δ2-hexanol) and formation of 2-hexanone, while accounting for differences in the FID response factors for the alcohol (1.1) versus the ketone (1.0) (24). The average organonitrate branching ratio for the hydroxyperoxy radicals was determined as:

$$\text{BR}_{\text{RONO}_2} = \frac{\Delta\text{RONO}_2}{\Delta 2\text{-hexanol} \times (1 - Y_{\text{ketone}})}$$

The results are shown in Table S2, and the error bounds reflect uncertainty in the calibration factors as well as measurement precision. The yield of 2-hexanone, Y_{ketone} , was determined to be 0.6 ± 0.2 , consistent with the expected value based on SAR estimates of the abstraction

preference (20, 21). Given the poor precision of the GC-FID measurements, the temperature dependence of the 2-hexanone yield was unresolved. The temperature dependence of BR_{RONO_2} is similar to that reported in Atkinson et al. for C_5 and C_7 alkanes (25).

Uncertainty

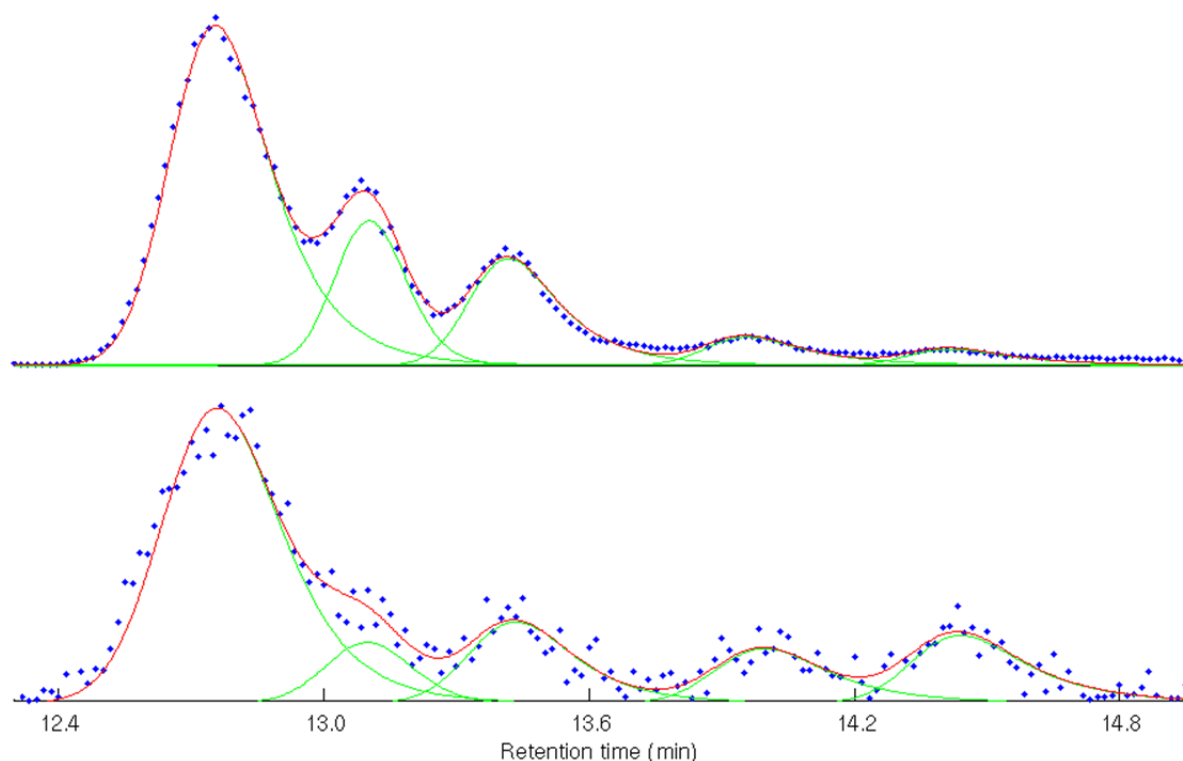


Figure S2. Representative chromatograms from a short (top, $\tau_{\text{bimolecular}} \approx 0.02$ s) and long (bottom, $\tau_{\text{bimolecular}} \approx 40$ s) lifetime experiment. The output of the peak deconvolution and fitting algorithm is shown for the peaks (green) and the sum (red). Background signals, particularly for the later eluting isomers, are apparent in the bottom chromatogram. These compounds have lower volatilities and persist in the experimental apparatus to a greater extent compared to the earlier eluting isomers.

There is significant uncertainty in our calculation of $\tau_{\text{bimolecular}}$ using observed production rates of the hydroperoxides and hydroxynitrates. We include the standard 1σ error incurred from the ordinary least-square fit to each production signal. Recommended rate coefficients also carry associated error. For example, $k_{\text{HO}_2} + k_{\text{HO}_2}$ carries a stated uncertainty of $\pm 15\%$ (17), while $k_{\text{RO}_2 + \text{NO}}$ and $k_{\text{RO}_2 + \text{HO}_2}$ presumably also carry uncertainty but the quantity is not provided in the literature (16). Furthermore, calibration factors are each estimated to carry $\pm 30\%$ uncertainty. In our calculation of $\tau_{\text{bimolecular}}$, the ratio of the RONO_2 and ROOH sensitivities is used; thus, the cumulative uncertainty in the calibration factors for this expression is $\sim 40\%$. In addition, the hot experiments saw the chamber temperature fluctuate on order $\pm 5^\circ\text{C}$.

As described in the main article, chromatography was used to quantify the isomers and determine the abundance of the 2,4 and 2,5 RONO₂ relative to that of the 2,3 RONO₂. Chromatographic challenges include poorly constrained peak shapes and sample backgrounds that contribute to error in the measured ratios of RONO₂. We studied the impact of different experimental conditions on the chromatography using the synthetic 2,5 RONO₂ standard. The peak shape of this single isomer is poorly represented by a Gaussian, as pronounced tailing is apparent. An Exponentially Modified Gaussian (EMG) provides a reasonable representation of the peak shape and was used to fit the chromatograms (26). We employed the peakfit.m function for Matlab by Dr. Tom O'Haver (27). The function was modified to enable treatment of the EMG with fixed peak widths and distinct tailing constants for each isomer. The output of the algorithm is shown for two representative chromatograms in Figure S2.

As the other RONO₂ isomers were not well separated, peak parameters were optimized as determined by the root mean square difference between the data and the EMG model. In minimizing the residuals, we found that the best fits were achieved when the isomers were allowed different tailing constants. Peak widths were also found to increase with collection time, consistent with the expected spread of the sample on the column. While these parameters were optimized to achieve the best fit, significant uncertainty existed due to the lack of authentic standards for each isomer.

In order to characterize the uncertainty, we used a bootstrapping method to probe the sensitivity of the isomer ratios to the assumed EMG peak parameters. In the bootstrap, we varied the peak widths and tailing constants by $\pm 40\%$ of the default choices (used, for example, in the fits shown in Figure S2). 10,000 fitting trials were used; further increases in the number of trials did not change the result, suggesting that the space was adequately sampled. Trials that degraded

the fit beyond 1σ of the root-mean-square error were rejected. The results of the bootstrap are summarized in Table S3.

Table S3. Bootstrap results expressed as % uncertainty (1σ) of measured RONO₂ isomer ratios resulting from the peak fits.

$\tau_{\text{bimolecular}} < 20 \text{ s}$		$\tau_{\text{bimolecular}} > 20 \text{ s}$	
2,4 RONO ₂ : 2,3 RONO ₂	2,5 RONO ₂ : 2,3 RONO ₂	2,4 RONO ₂ : 2,3 RONO ₂	2,5 RONO ₂ : 2,3 RONO ₂
16	12	25	14

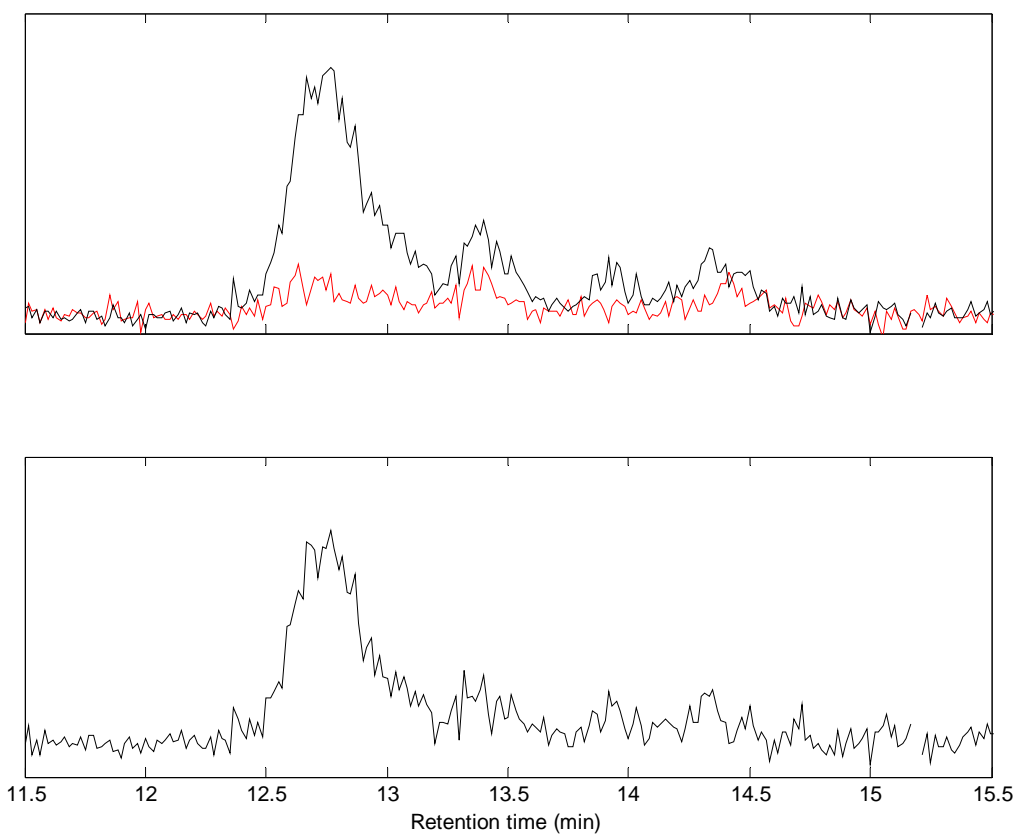


Figure S3. Top: a post-oxidation chromatogram (black) with the background (red) overlaid. Bottom: The background subtracted chromatogram. The data were extracted from an experiment at $\tau_{\text{bimolecular}} \approx 50 \text{ s}$.

At the longest lifetimes, an additional source of error arises from uncertainty in the background signals in the GC. Backgrounds were typically negligible ($< 5\%$ of post-oxidation

signal) for $\tau_{\text{bimolecular}} < 20$ s, but were quite significant (30% to 100% of post-oxidation signal) for long lifetime experiments. The uncertainty is further increased by low signal to noise. We show a background and post-oxidation chromatogram, along with the background subtracted signal, in Figure S3 for a long lifetime experiment. The isomers are retained differently in the experimental apparatus producing substantial variability in the backgrounds for long lifetime experiments. To bound the potential error in the measured RONO₂ isomer ratios due to these backgrounds, we collected several pre-oxidation chromatograms as well as zero air blanks following the conclusion of the experiment. We express the uncertainty (1σ) of the background peak areas at long lifetimes in the uncertainty range for these points.

A smaller source of uncertainty impacting longer $\tau_{\text{bimolecular}}$ data points arises from possible differences in our instrumental sensitivity toward the S,S vs. S,R stereoisomer. While a racemic mixture is assumed at the shortest lifetimes, our calculations show that this will not be the case as the RO₂ lifetimes increase, as indicated by the distinct rate constants for the diastereomers of the 2,5 RO₂. This effect has the potential to influence the distribution of RONO₂ we measure in our GC, as the column used here is not able to separate these diastereomers. We have bounded this effect by calculating the difference in instrumental sensitivity between the RONO₂ isomers, and we display the results in Table S1. The calculated sensitivities did not appreciably differ for any pair of diastereomers.

The determination of the experimental factor by fitting the data points with a model carries additional uncertainty. The experimental factor represents the value that, when multiplied by the calculated rate coefficient, afforded the best fit to the data. The same factor was used for both diastereomers. A weighted least squares approach was adopted to determine the best fit:

$$\sum_{i=1}^n \frac{1}{\sigma_i^2} (y_i - \hat{y}_i)^2$$

Where σ_i^2 represents the point-wise variance and $y_i - \hat{y}_i$ denotes the residual between the data points and the model. A Monte Carlo method was used in order to estimate the uncertainty in the fit. 5,000 synthetic data sets were generated, with each point lying within its respective range of uncertainty. The same procedure of weighted least squares was used to determine the best fit for each of the synthetic data sets. The error bounds provided with the experimental factors represent the full range of results that yielded a best fit to the synthetic data sets.

Computational methods

We followed the approach described by Møller et al. (28) and only a brief description is provided here. A sample TS conformer of the desired reaction was optimized with B3LYP/6-31+G(d) (abbreviated as B3LYP) in Gaussian 09 Rev. D. (29-34). That geometry was used as the input for a systematic conformer search in Spartan'14 with the MMFF force field (35-41). The TS conformer search was performed with the O-O, O...H and C-H bond distances locked. The input for the conformer search of the reactant and product were drawn in Spartan'14. In all of the conformer searches the MMFF force field was altered to enforce the correct charge on the radical center, with the keyword 'FFHINT=X~~+0' where X is the atom number of the radical. The resulting conformers were transferred to Gaussian 09, where constrained optimizations with B3LYP were performed for the TS conformers. The same constraints as in the conformer search were used. Afterwards, free optimizations for a saddle point were performed for the TS with B3LYP. The reactant and product were optimized for a minimum, also with B3LYP. The conformers were sorted according to electronic energy, and those within 2 kcal/mol of the lowest

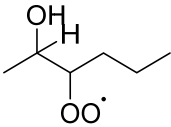
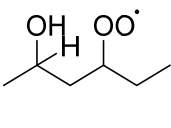
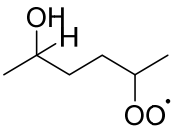
energy conformer were reoptimized with ω B97X-D/aug-cc-pVTZ (ω B97X-D) (42, 43). Their frequencies were calculated at the ω B97X-D level of theory as well. For the lowest zero-point-energy corrected conformer of the reactant, TS, and product, a single point energy calculation was performed in Molpro 2012.1 at the ROHF-ROCCSD(T)-F12a/VDZ-F12// ω B97X-D level of theory (F12) for an accurate value of $E_{TS,0}$ and $E_{R,0}$ (44-49).

We used the lowest energy TS conformer at the ω B97X-D level of theory for the Eckart tunneling correction (50). An intrinsic reaction coordinate (IRC) calculation was performed starting from the corresponding B3LYP TS structure in both the forward and back reaction. The endpoints of the IRC were optimized and then reoptimized with ω B97X-D, and F12 single point energy calculations were performed at the final ω B97X-D geometry.

Output files from the ω B97X-D and F12 calculations are available electronically at: <http://www.erda.dk/public/archives/YXJJaGl2ZS1JX1ZJSHA=/published-archive.html>

Expression of the rate coefficients

Table S4. Temperature dependence of the calculated rate coefficients.

Reactant		k (s^{-1})
	S,R	$1.5017 \times 10^{12} \times \exp\left(\frac{-13091}{T}\right) \times \exp\left(\frac{1.6504 \times 10^8}{T^3}\right)$
	S,S	$1.7506 \times 10^{12} \times \exp\left(\frac{-13488}{T}\right) \times \exp\left(\frac{1.5832 \times 10^8}{T^3}\right)$
	S,R	$5.0180 \times 10^{11} \times \exp\left(\frac{-9517.1}{T}\right) \times \exp\left(\frac{8.1948 \times 10^7}{T^3}\right)$
	S,S	$1.9370 \times 10^{12} \times \exp\left(\frac{-10084}{T}\right) \times \exp\left(\frac{9.2686 \times 10^7}{T^3}\right)$
	S,R	$9.1036 \times 10^{10} \times \exp\left(\frac{-8688.0}{T}\right) \times \exp\left(\frac{7.5470 \times 10^7}{T^3}\right)$
	S,S	$7.7343 \times 10^{10} \times \exp\left(\frac{-9144.2}{T}\right) \times \exp\left(\frac{7.5879 \times 10^7}{T^3}\right)$

The expressions in Table S4 were obtained using data calculated at 5 K intervals in the range 290 K-320 K. The MC-TST rate coefficients without tunneling were plotted against $1/T$ and were fit with an exponential function. The Eckart tunneling correction factor was plotted against $1/T^3$ and fit to an exponential. The pre-exponential factor in the rate expressions are the product of the pre-exponential factors in the two fits. Within the specified temperature range, the fits reproduce the calculated MC-TST rate constants, including tunneling, to within 0.5%.

Uncertainty

The uncertainty in the calculated rate coefficients originates from three parts of the MC-TST equation: the barrier height, the tunneling correction, and the partition functions. Werner et al. reports reaction energies calculated with CCSD(T)-F12a/VDZ-F12 for a set of 104 reactions with a mean average deviation of 0.70 kcal/mol from CCSD(T)/CBS results (51). The reactions studied by Werner et al. include primary small open- and closed-shell molecules. Some include second row atoms, but none of the reactions are unimolecular isomerizations. Møller et al. (28) reported barrier heights with CCSD(T)-F12a/VDZ-F12 to differ only by 0.25 and 0.33 kcal/mol from values obtained with CCSD(T)-F12/VDZ-F12// ω B97X-D/aug-cc-pVTZ. The latter is the same used in this study, and the reaction studied by Møller et al. is also a peroxy radical H-shift. We thus assign an uncertainty of 0.7 kcal/mol in the barrier heights, which would translate to a factor of 3 uncertainty in the rate coefficient at 298 K.

Sha and Dibble (52) reported a ratio between the Eckart tunneling correction and the microcanonically optimized multidimensional tunneling correction (μ OMT) of 1.7 for a peroxy radical H-shift. Zhang and Dibble (53) reported ratios of 0.74 and 2.3 between the Eckart correction and small-curvature tunneling (SCT). All three ratios are at 300 K and calculated as the Eckart correction divided by either SCT or μ OMT. μ OMT is a more advanced approach than

SCT as it includes effects from large-curvature tunneling (LCT) which leads to a higher value for the tunneling correction. As such, we assign a factor of 2 uncertainty in the rate constant at 298 K stemming from the tunneling estimate.

Since our approach to MC-TST includes a cut-off after B3LYP optimizations, where only the conformers within 2 kcal/mol of the lowest in energy are kept, we introduce an imprecision in the sum of partition functions. Møller et al. reported the error to be smaller than 20% for both the forward and reverse rate constant of four different reactions (28). We used the harmonic oscillator (HO) approximation, which poorly reproduces the barrier to internal torsions, leading to an error in the partition functions used for the rate constants. Zhang and Dibble reported differences up to a factor of five at 300 K between rate constants calculated with harmonic oscillator and hindered rotor (HR) approximations, respectively (53). Lin et al. showed HO partition functions that deviated by 28% compared to values obtained with torsional eigenvalue summation (54). Some of this effect is expected to cancel, as hindered rotors are likely present in both the reactant and TS. Møller et al. showed that using the HR approximations implemented in Gaussian 09 had little effect on their system, with differences no larger than 33% at 298 K (28). Based on these reports we estimate our combined uncertainty from the cutoff and hindered rotations to be a factor of 2.

All of these factors combined would lead to a total uncertainty in the rate coefficient of a factor of 12. However, some of the effects (e.g. barrier height and tunneling) would likely cancel which leads us to estimate a factor of 10 uncertainty in the absolute values of the rate coefficients. However, previous applications of the approach used here produce agreement with experiment to better than a factor of five (28), a trend that is continued in this work. Since these uncertainties probably affect our rate coefficients in similar manners, the calculated rate

coefficients are likely more accurate relative to each other. Increasing temperature changes the accuracy of the different approximations, HR becomes more important, and tunneling becomes less important. However, the temperature range considered here is likely too narrow to have a considerable effect on our uncertainty estimates.

High temperature data (318 K)

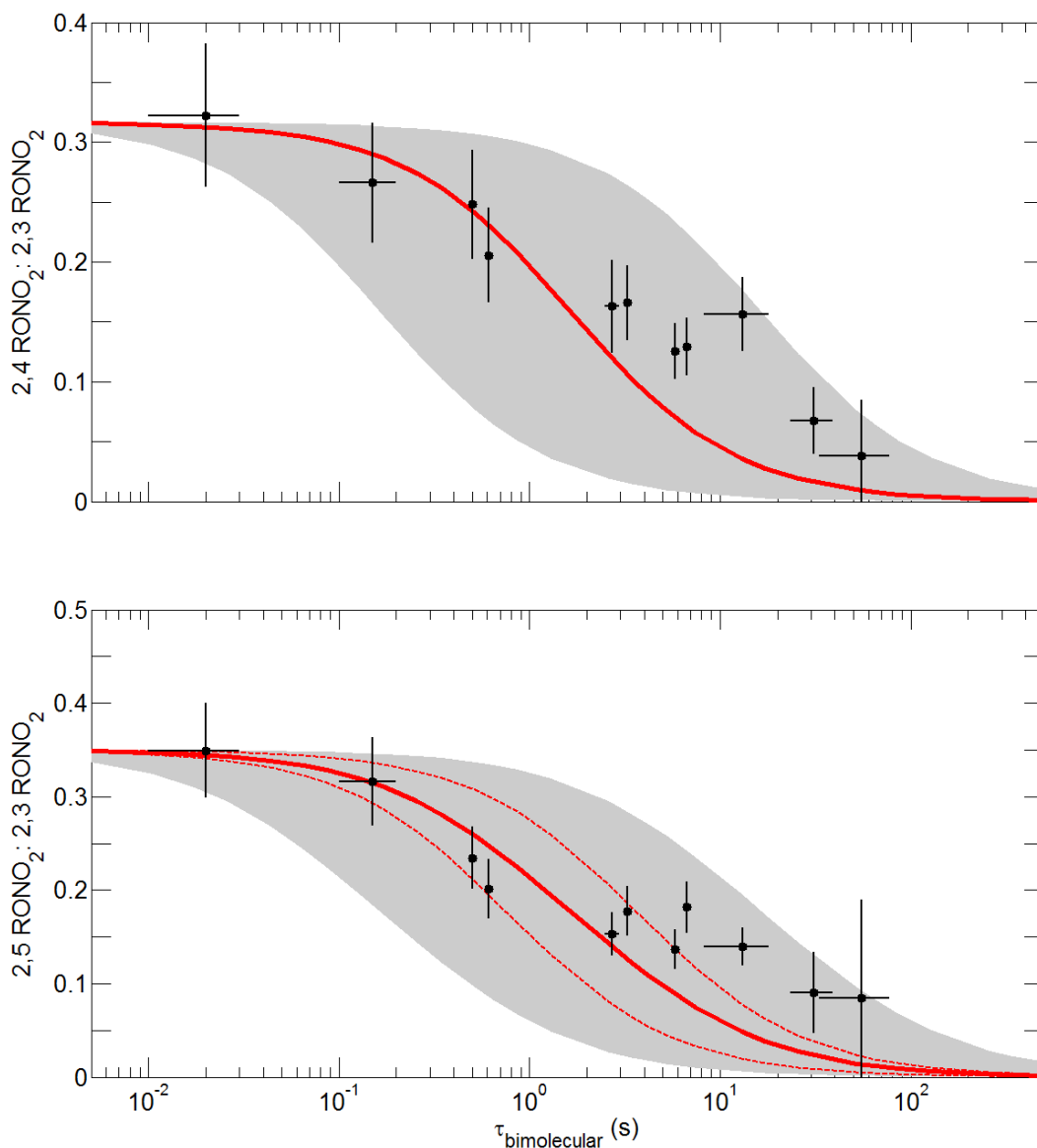


Figure S4. Comparison of experimental (black dots) and computational (red lines) results at 318 K. We demonstrate the difference between S,R and S,S for the 2,5 RO₂ H-shift in the two dashed red lines that, when combined assuming a racemic mixture, produce the solid red line. The gray shaded region represents the range of uncertainty in the calculated rate coefficients.

As discussed in the main article, we observe a significant decrease in the lifetimes of the 2,4 and 2,5 RO₂ at 318 K. This decrease is consistent with the expectation that the rate of autoxidation increases with temperature (55), and provides confidence in our interpretation of the mechanism.

The large scatter in the data compared to the data at 296 K is due, in part, to temperature fluctuations (± 5 K) as well as increased water vapor diffusing into the chamber.

Deuterated 2-hexanol

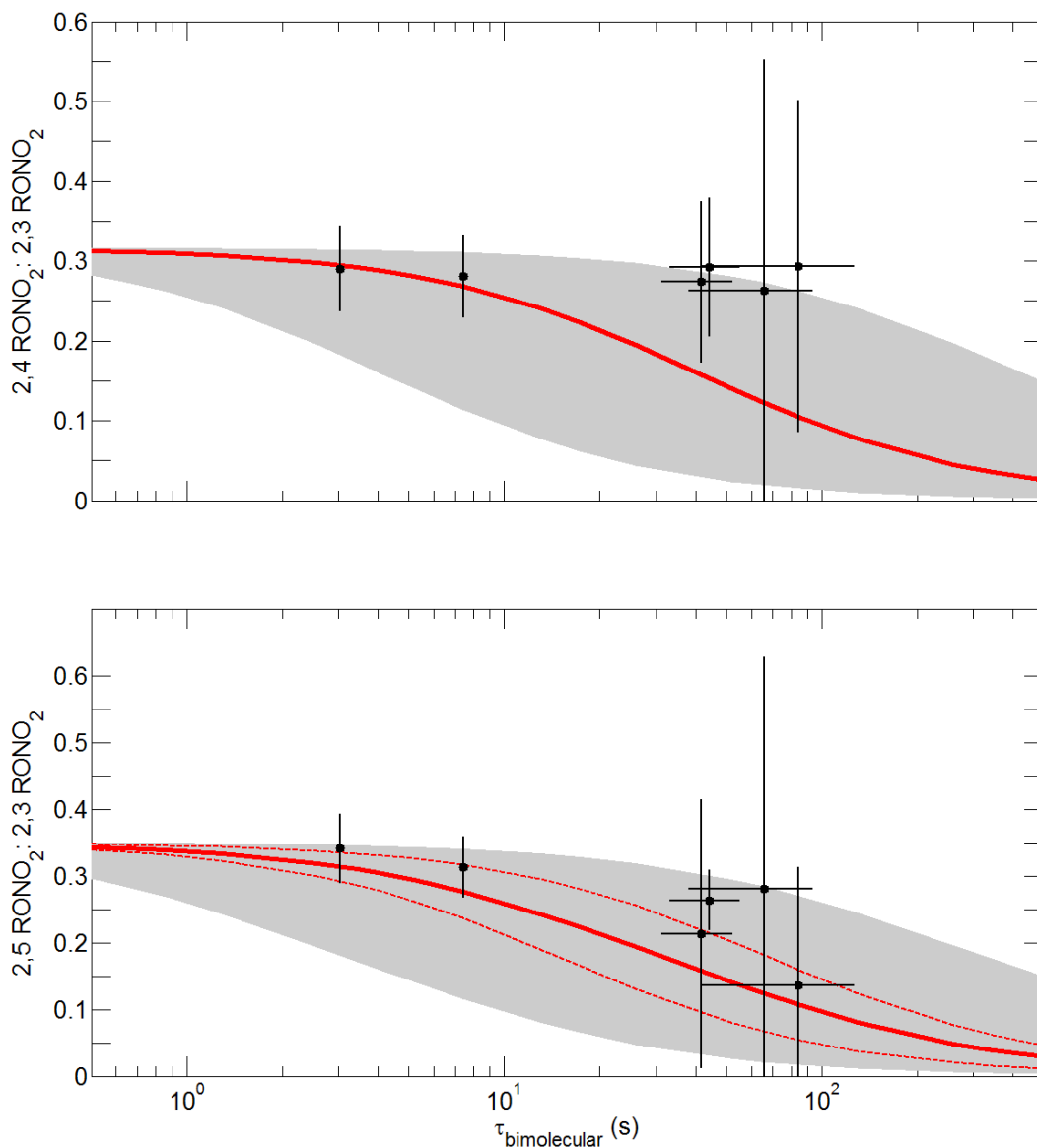
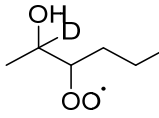
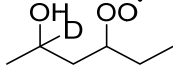
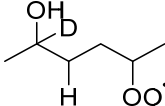


Figure S5. Comparison of experimental (black dots) and computational (red lines) results at 318 K for the deuterated compound. We demonstrate the difference between S,R and S,S for the 1,5 and 1,6 H-shifts of the 2,5 RO₂ in the two dashed red lines that, when combined assuming a racemic mixture, produce the solid red line. The gray shaded region represents the range of uncertainty in the calculated rate coefficients.

Table S5. D(H)-shift rates (s^{-1}) and factors derived from theory and experiment, respectively, for deuterated 2-hexanol. Rate coefficients are calculated following the approach by Møller *et al.* at the CCSD(T)-F12a/cc-pVDZ-F12// ω B97X-D/aug-cc-pVTZ level of theory (28).

Reactant						
D(H)-shift		1,4	1,5	1,5	1,6	
298 K	Theory ^a	S,R	4.3×10^{-7}	4.7×10^{-3}	2.9×10^{-4}	0.012
		S,S	1.2×10^{-7}	3.3×10^{-3}	2.0×10^{-4}	2.3×10^{-3}
318 K	Theory ^a	S,R	4.3×10^{-6}	0.028	1.9×10^{-3}	0.063
		S,S	1.3×10^{-6}	0.021	1.3×10^{-3}	0.013
	Expt. (factor) ^b	-	< 0.2 +0.8/-0.2	0.3 +0.6/-0.2		

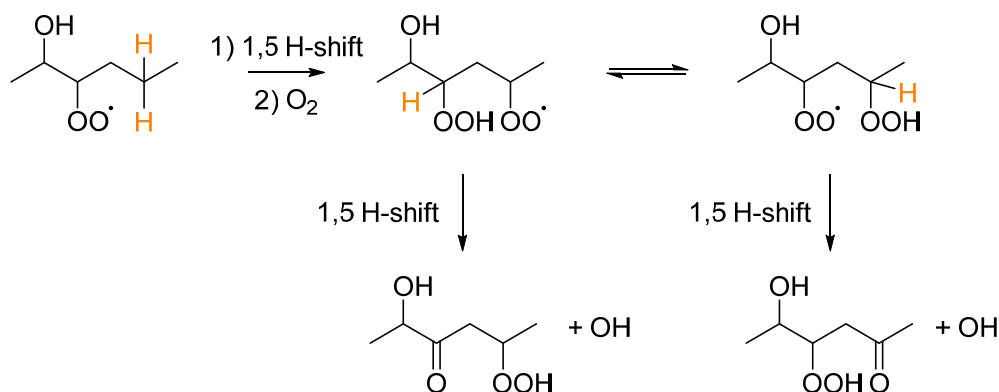
^a Uncertainty in the calculated rates is estimated to be a factor of ~ 10

^b Reported values correspond to scaling factors that afforded the best fit to the experimental data. The experiments are unable to differentiate the S,R and S,S isomers, nor can they distinguish the 1,5 and 1,6 H-shifts from the 2,5 RO₂

Consistent with the proposed mechanism, we observe a primary kinetic isotope effect (KIE) following deuterium substitution at the α -OH center (HOC-D). We employed the same experimental method at 318 K for the deuterated substrate to estimate the KIE, and display the results in Figure S5 and Table S5. The best fits to the experimental data are displayed in Figure S10. The calculations suggest that the observed decrease in the RO₂ D-shift rate coefficient is due to a decrease in tunneling by a factor of 4–17 and a seemingly systematic ~ 1 kcal/mol increase in barrier height.

While the ketohydroperoxide product at m/z 217 continued to dominate in the D-substitution experiments, the formation of m/z 234 was enhanced compared to the formation of m/z 233 in H-substitution experiments at similar $\tau_{\text{bimolecular}}$. For two experiments at

$\tau_{\text{bimolecular}} \sim 7$ s, m/z 234: m/z 217 ~ 0.25 (D-substitution) while m/z 233: m/z 217 < 0.10 (H-substitution). This signal is consistent with a hydroxy ketohydroperoxide product, which we suspect results from successive 1,5 H-shifts from both the 2,5 RO₂ (Scheme 4, main article) and 2,3 RO₂ (Scheme S1). Calculation of the 1,5 H-shift rate coefficient from the 2,3 RO₂ was not undertaken in this work. However, previous studies have estimated the rate coefficient in similar systems to be of the same order as the 1,5 H-shift from the 2,5 RO₂ reported in Table S5 (13, 66).



Scheme S1. An additional route to hydroxy ketohydroperoxides with the 2,3 RO₂ as the precursor. Hydrogen atoms involved in the H-shifts are orange highlighted.

Diastereomer effects

As can be seen from Table S6, there is a 1 kcal/mol difference in the barrier height for the 1,6 H-shift of the S,R and S,S isomer of the 2,5 RO₂. The tunneling corrections are very similar, as are the ratios between the partition functions of the TS conformers and reactant conformers. Thus, the difference in barrier height is almost solely responsible for the factor of ~ 5 difference in the rate coefficients (see main article).

In the case of the 1,4 H-shift of the 2,3 RO₂, there is a factor of ~ 4 difference in the rate coefficient between the S,R and S,S isomer. The barrier height is ~ 0.5 kcal/mol lower for the S,R isomer, which increases the rate coefficient. A further increase for the S,R isomer is attained by a

greater ratio between the partition functions as well as a higher tunneling correction factor, and cannot solely be ascribed to differences in the barrier height as for the 2,5 RO₂ system.

Table S6. Barrier heights, ratios between partition functions and Eckart tunneling correction factors for the reactions studied here. Calculated following the approach of Møller *et al.* at the CCSD(T)-F12a/cc-pVDZ-F12// ω B97X-D/aug-cc-pVTZ level of theory at 298 K (28).

Reaction	Isomer	$E_{TS,0} - E_{R,0}$ (kcal/mol)	$\frac{\sum_i^{TS\ conf.} \exp\left(\frac{-\Delta E_i}{k_B T}\right) Q_{TS,i}}{\sum_j^{R\ conf.} \exp\left(\frac{-\Delta E_j}{k_B T}\right) Q_{R,j}}$	κ_{Eckart}	$k_{H-shift}$ (s ⁻¹)
1,4 H-shift	(S,R) 2,3 RO ₂	26.08	0.225	606	6.5×10 ⁻⁵
	(S,S) 2,3 RO ₂	26.52	0.145	473	1.6×10 ⁻⁵
1,5 H-shift	(S,R) 2,4 RO ₂	18.98	0.044	45	0.15
	(S,S) 2,4 RO ₂	20.29	0.243	65	0.13
1,6 H-shift	(S,R) 2,5 RO ₂	17.60	0.011	40	0.35
	(S,S) 2,5 RO ₂	18.64	0.011	43	0.065

The 1,5 H-shift of the 2,4 RO₂ exhibits virtually identical rate constants for the S,R and S,S isomers. Again, the barrier height is lower for the S,R isomer, this time by ~1.3 kcal/mol. However, the ratio of the partition functions is low for the S,R isomer, because of a high number of low-energy reactant conformers. That is not the case for the S,S isomer where the ratio is higher by a factor of ~6. Additionally, the tunneling correction factor is ~50% larger for the S,S isomer. When these three effects are combined, the rate constants are nearly identical at 0.13 s⁻¹ and 0.11 s⁻¹ (T=296 K) for the S,R and S,S isomer, respectively. We display the geometries of the lowest lying conformers of the reactant and TS of the 1,4 H-shift of the 2,3 RO₂ (Figure S6) and the 1,5 H-shift of the 2,4 RO₂ (Figure S7). Refer to the main article (Figure 3) for the geometries of the 1,6 H-shift of the 2,5 RO₂. By visual inspection, it is understandable that the barrier height is lower for the S,R isomer. For all three systems, hydrogen bond-like interactions serve to either stabilize the reactant of the S,S isomer or the TS of the S,R isomer. Both lead to a lower barrier height for the S,R isomer relative to the S,S isomer.

Best fits

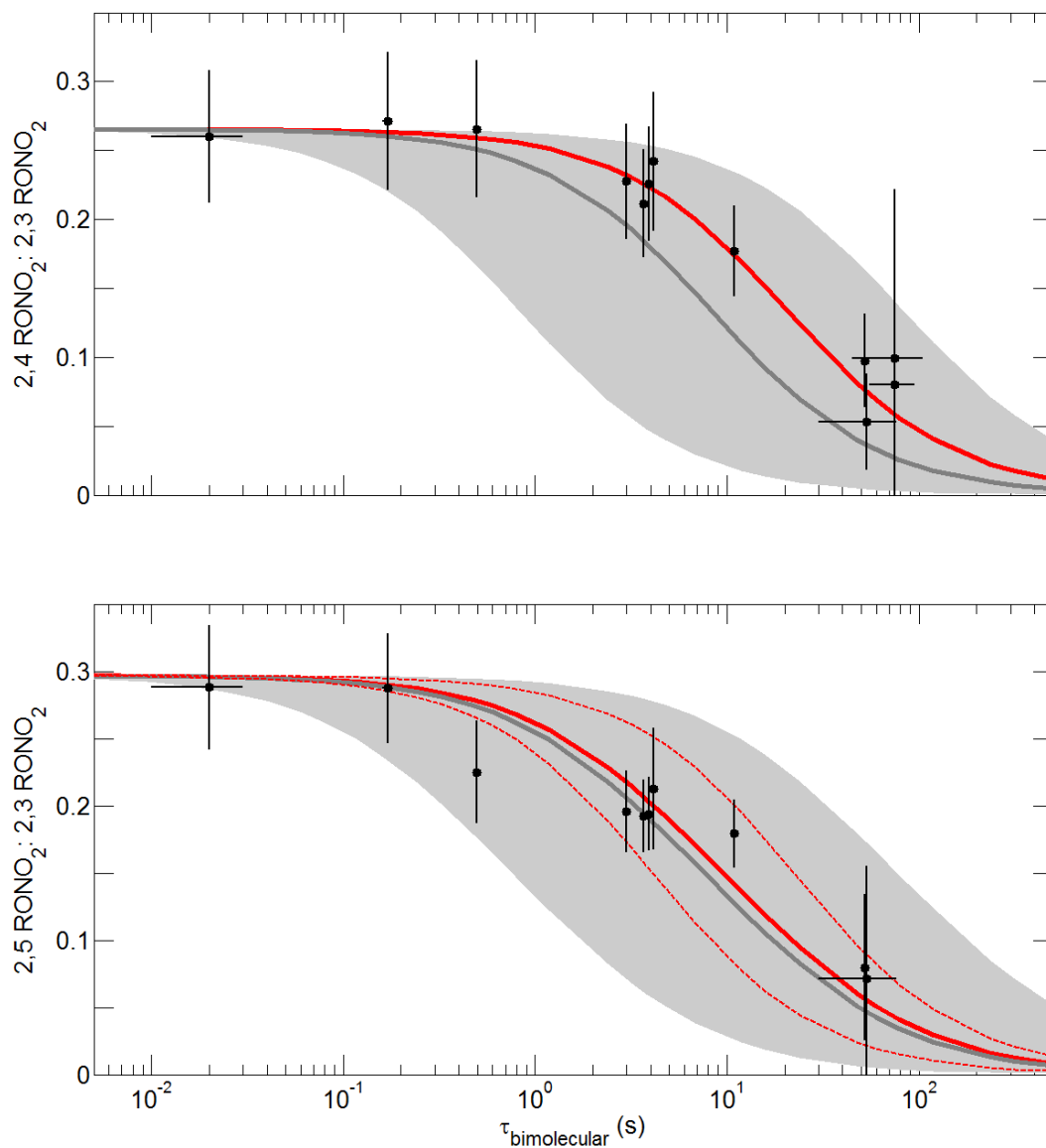


Figure S8. Best fits are shown for the 2-hexanol data at 296 K. Simulated curves (red lines) were generated by multiplying the calculated rate coefficients by the experimental factors displayed in Table 1. The gray line represents the result obtained using the calculated rate coefficients. The solid lines assume a racemic mixture, while the dashed lines assume either entirely S,R or entirely S,S.

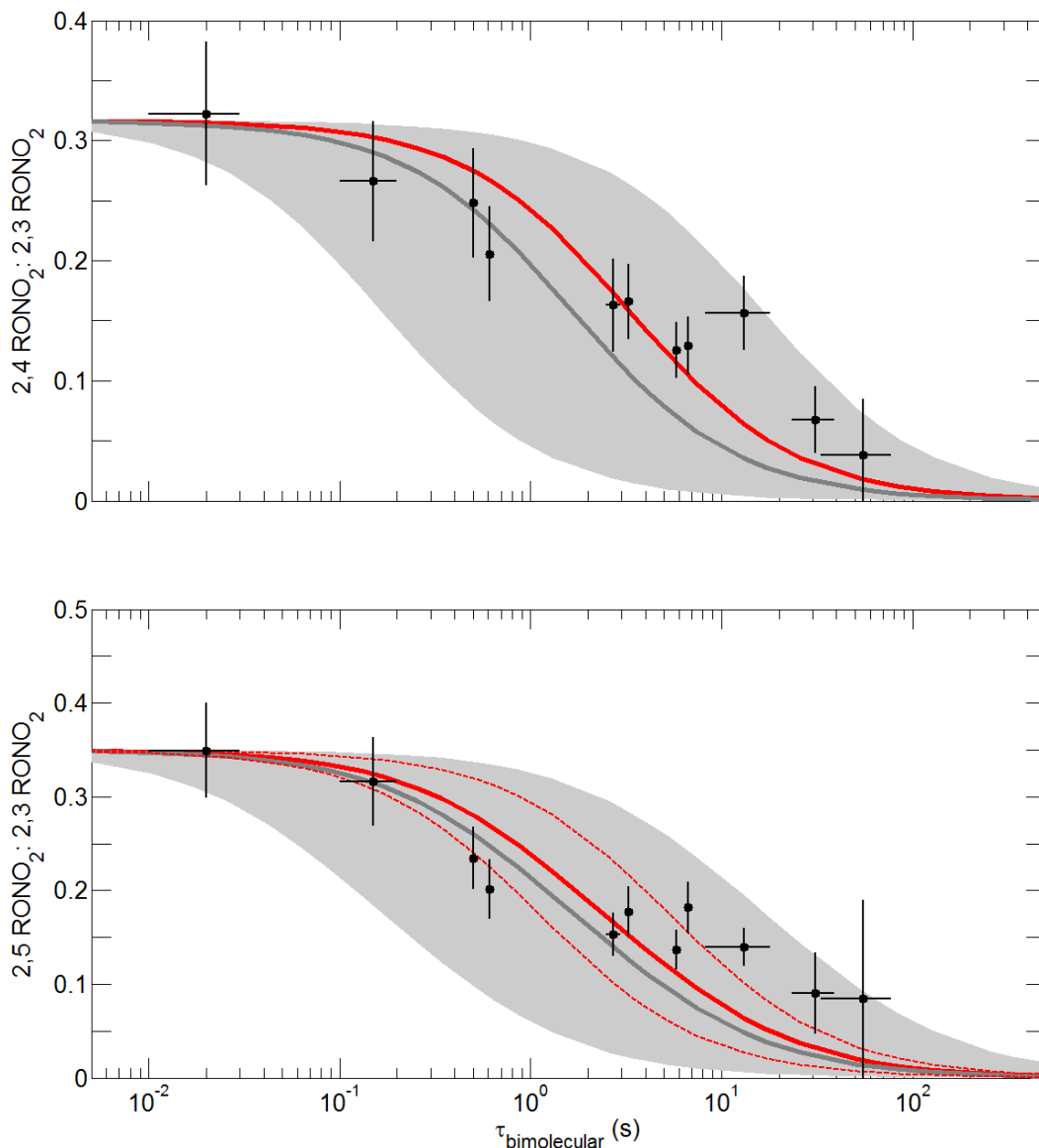


Figure S9. Best fits are shown for the 2-hexanol data at 318 K. Simulated curves (red lines) were generated by multiplying the calculated rate coefficients by the experimental factors displayed in Table 1. The gray line represents the result obtained using the calculated rate coefficients. The solid lines assume a racemic mixture, while the dashed lines assume either entirely S,R or entirely S,S.

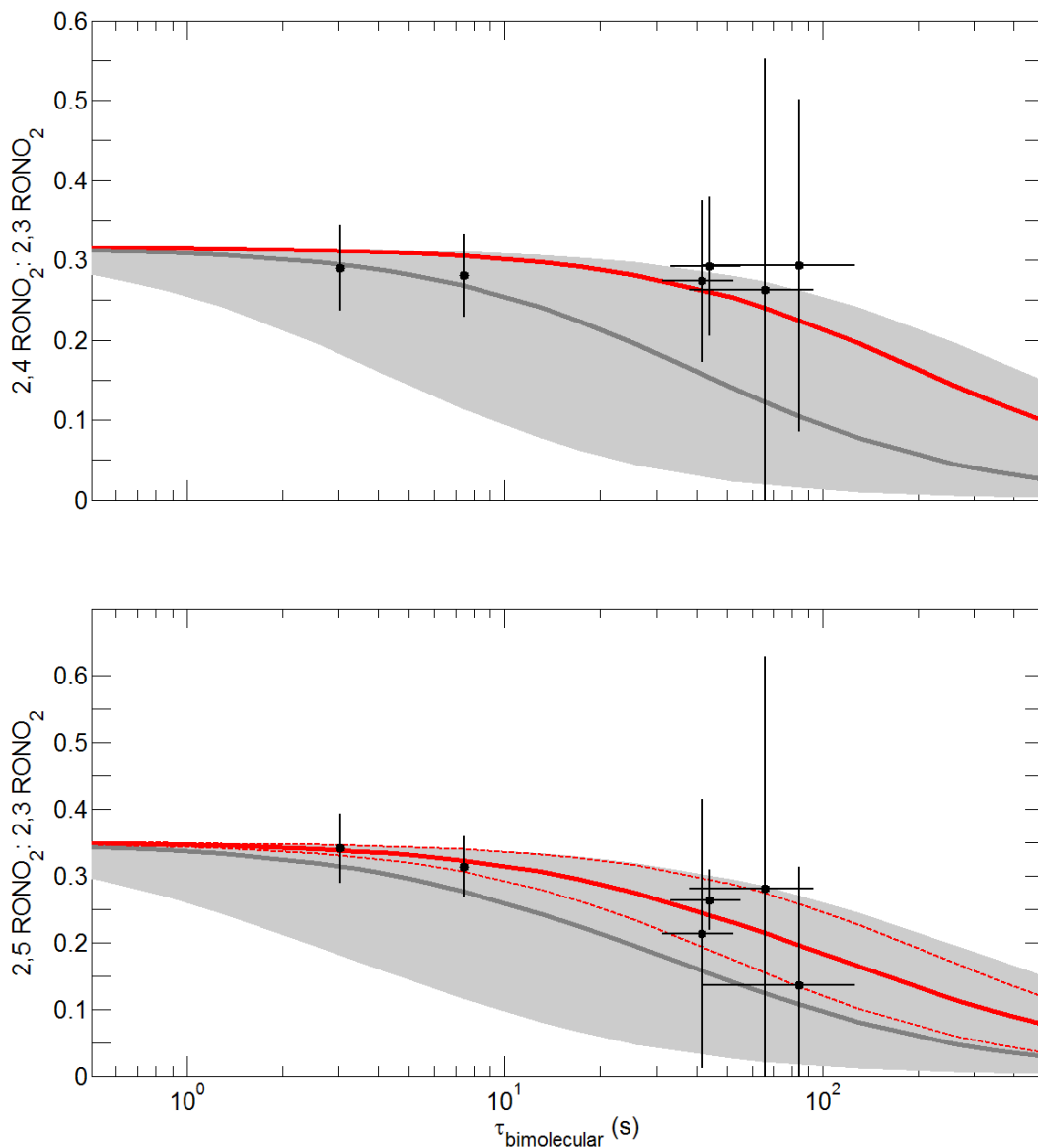
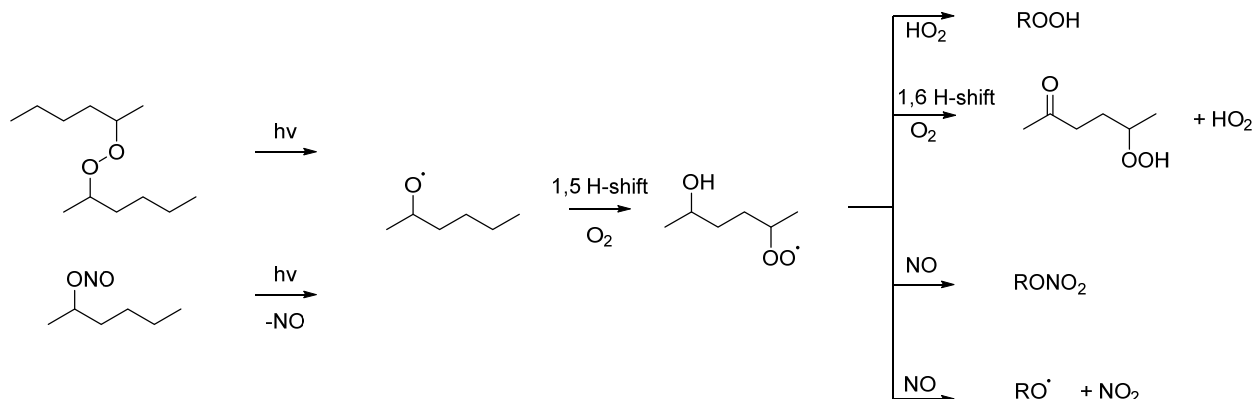


Figure S10. Best fits are shown for deuterated 2-hexanol at 318 K. Simulated curves (red lines) were generated by multiplying the calculated rate coefficients by the experimental factors displayed in Table S5. The gray line represents the result obtained using the calculated rate coefficients. The solid lines assume a racemic mixture, while the dashed lines assume either entirely S,R or entirely S,S.

Previous determination of the 1,6 RO₂ H-shift



Scheme S2. Mechanism to produce the 2,5 hydroxy RO₂ using bis-hexylperoxide and 2-hexylnitrite precursors.

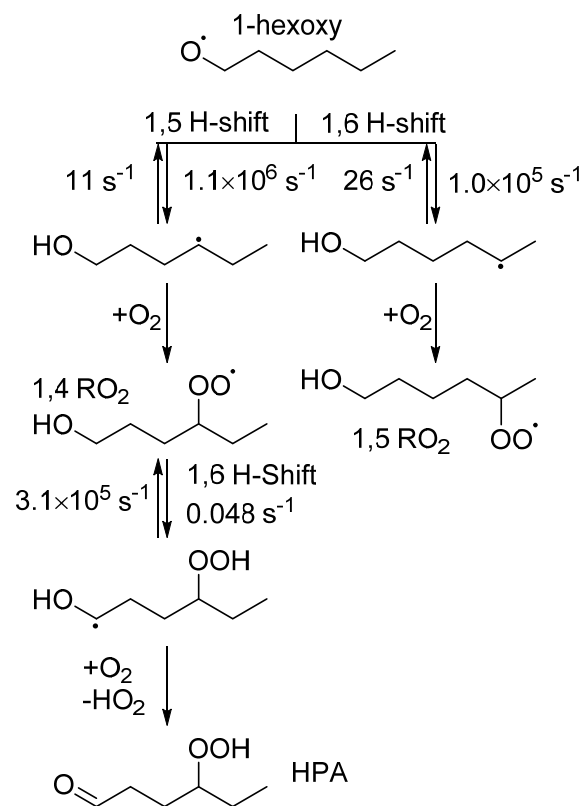
Jorand et al. previously reported rate coefficients for the 1,6 H-shift in this system at elevated temperatures (453 and 483 K) (56). To form the 2,5 RO₂ radical, di-2-hexylperoxide was pyrolyzed to produce the same RO₂ that undergoes the 1,6 H-shift reported here. For the very fast H-shift rates ($\sim 10^3 \text{ s}^{-1}$) observed at these temperatures, the peroxy radical lifetime is sufficiently short that RO₂ self-reactions are minimal despite the large RO₂ concentrations produced.

In an attempt to replicate their method, we photolyzed both 2-hexylnitrite and di-2-hexylperoxide (hereafter, hexoxy method) as shown in Scheme S2. However, as our experiments were conducted at room temperature, we needed to significantly reduce the RO₂ concentrations to avoid self-reaction. We therefore used a much slower photolysis rate than the pyrolysis rate of Jorand et al. Additionally, we found that photolysis did not constitute the sole loss of starting material. OH-initiated oxidation represented a large fraction of the 2-hexylnitrite and di-2-hexylperoxide loss, which further muddled interpretation of the data. In addition, as the hexoxy method did not produce the suite of RONO₂ used here to diagnose the H-shift rate, our estimation of the rate coefficients in these experiments required absolute quantification of the

bimolecular and unimolecular products. As a result of these limitations, attempts to quantify the 1,6 H-shift rate coefficient via this method were inconsistent and prone to error.

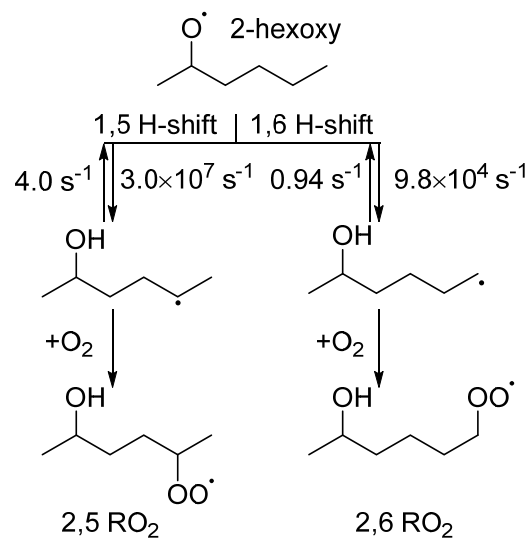
Calculations for the hexoxy method

While assessing the hexoxy chemistry in the laboratory, we completed a series of complementary calculations. Scheme S3 shows the fastest H-shift reactions of 1-hexoxy and its subsequent products. The rate coefficients shown are calculated following the MC-TST approach of Møller et al. used for the other rate coefficients presented in this work and are at the CCSD(T)-F12a/cc-pVDZ-F12// ω B97X-D/aug-cc-pVTZ level of theory (28). The reactions of R• with O₂ are assumed to be fast with a pseudo first-order rate coefficient of $1.2 \times 10^7 \text{ s}^{-1}$. This is based on a second-order rate coefficient of $2.3 \times 10^{12} \text{ cm}^3 \text{ molecule}^{-1} \text{ s}^{-1}$ and an O₂ concentration of $5.3 \times 10^{18} \text{ molecule cm}^{-3}$ (21% O₂ by volume at P=760 torr) (57, 58).



Scheme S3. H-Shift reactions of 1-hexoxy and its H-shift products. Rate coefficients are calculated with MC-TST and CCSD(T)-F12a/VDZ-F12// ω B97X-D/aug-cc-pVTZ.

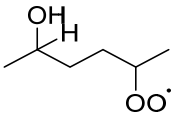
As can be seen from the forward rate coefficients in Scheme S3, 1-hexoxy is most likely to undergo a 1,5 H-shift. The reverse rate constants are too slow compared to the reaction with O_2 , leading to formation of the 1,4-hydroxy peroxy radical. The 1,6 H-shift of the 1,4-peroxy radical is the fastest H-shift of that species and forms a new alkyl radical, which finally forms a hydroperoxy-aldehyde (HPA) through H-abstraction by O_2 . HPA is expected to be the major autoxidation product of 1-hexoxy. According to the MC-TST rate coefficients of the 1,5 and 1,6 H-shift of 1-hexoxy, approximately 10% of 1-hexoxy reacts through a 1,6 H-shift. This finding nominally agrees with the alkoxy SAR of Vereecken et al. (59), and was corroborated in the laboratory. Generally, the alkoxy radicals are much more reactive than their peroxy counterparts, which is consistent with results in the literature (60, 61).



Scheme S4. H-Shift reactions of 2-hexoxy. Rate coefficients are calculated with MC-TST and CCSD(T)-F12a/VDZ-F12// ω B97X-D/aug-cc-pVTZ.

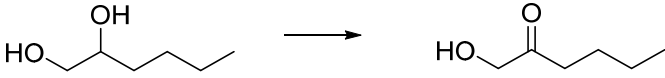
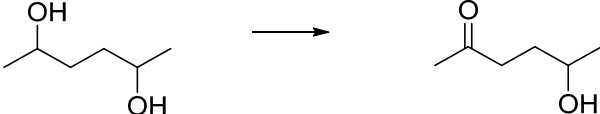
Scheme S4 shows the corresponding mechanism for 2-hexoxy. Based on the MC-TST rate coefficients, the 1,5 H-shift accounts for approximately 99% of all H-shift reactions, in agreement with the Vereecken et al. SAR (59). The 2,5 RO₂ is therefore expected to be the major autoxidation precursor, which can isomerize through a 1,6 RO₂ H-shift and form the ketohydroperoxide after reaction with O₂, as shown in the main article. In addition to the temperature range reported here, we calculated the 1,6 H-shift rate coefficient for the temperatures of the Jorand et al. experiments (Table S7). The approach of Møller et al. is optimized at 298 K and, due to hindered rotors and the conformer energy cutoff, becomes less reliable at elevated temperature (28). Nevertheless, reasonable agreement between theory and experiment is demonstrated.

Table S7. H-shift rate coefficients (s^{-1}) derived by theory and earlier experimental work (56). Rate coefficients are calculated following the approach of Møller et al. at the CCSD(T)-F12a/cc-pVDZ-F12// ω B97X-D/aug-cc-pVTZ level of theory.

		453 K	483 K
MC-TST	S,R	8.6×10^2	2.4×10^3
	S,S	2.5×10^2	7.4×10^2
Jorand et al. (2003)		$2.3 (+5.6/-1.8) \times 10^3$	$6.1 (+14/-4.8) \times 10^3$

Quantification of the 2,5 ketohydroperoxide

Table S8. Comparison of experimentally determined and predicted yields for hexanediol oxidation by OH.

reaction	SAR yield (20)	measured yield (approx.) ^b
	0.75 ^a	0.6 ^a
	0.85	< 0.1

^a The yield represents the sum of the two β -hydroxycarbonyl isomers

^b The yield was calculated by dividing the observed formation of the hydroxy carbonyl by the observed loss of the diol. We did not account for potential differences in sensitivity.

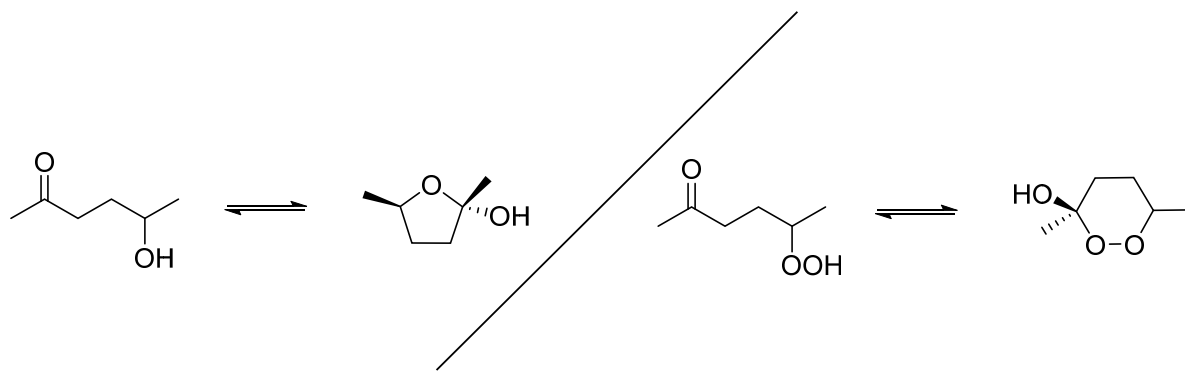


Figure S11. Depiction of the hypothesized cyclization process leading to hemiketal (left) and endoperoxide (right) formation.

One potential source of error in our determination of the H-shift rate using the hexoxy method is lack of carbon closure due to loss of the ketohydroperoxide. This could result, for example, from the formation of an endoperoxide (Figure S11). In a separate set of experiments, we found evidence that cyclization of 2,5 hydroxy ketones occurs. Following the oxidation of 2,5 hexanediol (see Table S8), the measured yield of 5-hydroxy-2-hexanone, the expected major product, was very low. This finding is consistent with hemiketal cyclization as depicted in Figure S11. This (likely heterogeneous) process has previously been suggested to occur in analogous systems (62, 63). In contrast, the observed hydroxy carbonyl yield following oxidation of 1,2 hexanediol was much higher (~ 0.6), consistent with the expectation that cyclization is minimal for β hydroxy carbonyls. The cyclic products possibly undergo CF_3O^- ion chemistry that results in fragmentation. The calculated sensitivity of the cyclic product was only a factor of 2 lower than the open-chain 5-hydroxy-2-hexanone. The greater than factor of 6 discrepancy in the measured yield is consistent with instrumental quantification challenges.

A similar mechanism is suspected of converting the 2,5 ketohydroperoxide in the hexoxy experiments as demonstrated in previous work (64, 65). Using production rates of the ketohydroperoxide as observed at the CF_3O^- cluster mass (m/z 217), we infer substantially lower

H-shift rate coefficients (assuming a ketohydroperoxide yield of 1 following the RO₂ H-shift) than from the nitrate method. We were unable to locate ions consistent with a fragmentation process in the GC analyses suggesting that the products were undetected.

References

1. Sharpe SW, *et al.* (2004) Gas-phase databases for quantitative infrared spectroscopy. *Appl. Spectrosc.* 58(12):1452-1461.
2. Meddour A, Atkinson D, Loewenstein A, & Courtieu J (1998) Enantiomeric analysis of homologous series of secondary alcohols by deuterium nmr spectroscopy in a chiral nematic liquid crystal: Influence of molecular geometry on chiral discrimination. *Chem. Eur. J.* 4(7):1142-1147.
3. Taylor WD, *et al.* (1980) Atmospheric photo-dissociation lifetimes for nitromethane, methyl nitrite, and methyl nitrate. *Int. J. Chem. Kinet.* 12(4):231-240.
4. Muthuramu K, Shepson PB, & O'Brien JM (1993) Preparation, analysis, and atmospheric production of multifunctional organic nitrates. *Environ. Sci. Technol.* 27(6):1117-1124.
5. Bates KH, *et al.* (2014) Gas phase production and loss of isoprene epoxydiols. *J. Phys. Chem. A* 118(7):1237-1246.
6. Crouse JD, McKinney KA, Kwan AJ, & Wennberg PO (2006) Measurement of gas-phase hydroperoxides by chemical ionization mass spectrometry. *Anal. Chem.* 78(19):6726-6732.
7. Paulot F, *et al.* (2009) Isoprene photooxidation: new insights into the production of acids and organic nitrates. *Atmos. Chem. Phys.* 9(4):1479-1501.
8. Teng AP, *et al.* (2014) Hydroxy nitrate production in the OH-initiated oxidation of alkenes. *Atmos. Chem. Phys. Discuss.* 14(5):6721-6757.
9. St. Clair JM, *et al.* (2016) kinetics and products of the reaction of the first-generation isoprene hydroxy hydroperoxide (ISOPOOH) with OH. *J. Phys. Chem. A* 120(9):1441-1451.
10. Teng AP, Crouse JD, & Wennberg PO (2017) Isoprene peroxy radical dynamics. *J. Am. Chem. Soc.* 139(15):5367-5377.
11. Praske E, *et al.* (2015) Atmospheric fate of methyl vinyl ketone: Peroxy radical reactions with NO and HO₂. *J. Phys. Chem. A* 119(19):4562-4572.
12. Teng AP, Crouse JD, & Wennberg PO (2017) Isoprene peroxy radical dynamics. *J. Am. Chem. Soc.* 139(15):5367-5377.
13. Crouse JD, *et al.* (2012) Atmospheric fate of methacrolein. 1. Peroxy radical isomerization following addition of OH and O₂. *J. Phys. Chem. A* 116(24):5756-5762.
14. Crouse JD, Nielsen LB, Jørgensen S, Kjaergaard HG, & Wennberg PO (2013) Autoxidation of organic compounds in the atmosphere. *J. Phys. Chem. Lett.* 4(20):3513-3520.
15. Crouse JD, Paulot F, Kjaergaard HG, & Wennberg PO (2011) Peroxy radical isomerization in the oxidation of isoprene. *Phys. Chem. Chem. Phys.* 13(30):13607-13613.

16. Saunders SM, Jenkin ME, Derwent RG, & Pilling MJ (2003) Protocol for the development of the Master Chemical Mechanism, MCM v3 (Part A): tropospheric degradation of non-aromatic volatile organic compounds. *Atmos. Chem. Phys.* 3:161-180.
17. Atkinson R, *et al.* (2004) Evaluated kinetic and photochemical data for atmospheric chemistry: Volume I - gas phase reactions of O_x, HO_x, NO_x and SO_x species. *Atmos. Chem. Phys.* 4:1461-1738.
18. Su T & Chesnavich WJ (1982) Parametrization of the ion-polar molecule collision rate-constant by trajectory calculations. *J. Chem. Phys.* 76(10):5183-5185.
19. Garden AL, *et al.* (2009) Calculation of conformationally weighted dipole moments useful in ion-molecule collision rate estimates. *Chem. Phys. Lett.* 474(1-3):45-50.
20. Kwok ESC & Atkinson R (1995) Estimation of hydroxyl radical reaction rate constants for gas-phase organic compounds using a structure-reactivity relationship: An update. *Atmos. Environ.* 29(14):1685-1695.
21. Bethel HL, Atkinson R, & Arey J (2001) Kinetics and products of the reactions of selected diols with the OH radical. *Int. J. Chem. Kinet.* 33(5):310-316.
22. Begum S & Subramanian R (2014) Reaction of chlorine radical with tetrahydrofuran: a theoretical investigation on mechanism and reactivity in gas phase. *J Mol Model* 20(6):1-11.
23. Atkinson R, *et al.* (2006) Evaluated kinetic and photochemical data for atmospheric chemistry: Volume II - gas phase reactions of organic species. *Atmos. Chem. Phys.* 6:3625-4055.
24. Scanlon JT & Willis DE (1985) Calculation of flame ionization detector relative response factors using the effective carbon number concept. *J. Chromatogr. Sci.* 23(8):333-340.
25. Atkinson R, Carter WPL, & Winer AM (1983) Effects of temperature and pressure on alkyl nitrate yields in the NO_x photooxidations of normal-pentane and normal-heptane. *J. Phys. Chem.* 87(11):2012-2018.
26. Jeansonne MS & Foley JP (1991) Review of the Exponentially Modified Gaussian (EMG) function since 1983. *J. Chromatogr. Sci.* 29(6):258-266.
27. O'Haver T (2016) Interactive Peak Fitter. Available at <https://terpconnect.umd.edu/~toh/spectrum/InteractivePeakFitter.htm>. Accessed January 8, 2017.
28. Møller KH, Otkjær RV, Hyttinen N, Kurtén T, & Kjaergaard HG (2016) Cost-effective implementation of multiconformer transition state theory for peroxy radical hydrogen shift reactions. *J. Phys. Chem. A* 120(51):10072-10087.
29. Becke AD (1993) Density-functional thermochemistry. III. The role of exact exchange. *J. Chem. Phys.* 98(7):5648-5652.
30. Lee C, Yang W, & Parr RG (1988) Development of the Colle-Salvetti correlation-energy formula into a functional of the electron density. *Phys. Rev. B* 37(2):785-789.
31. Hehre WJ, Ditchfield R, & Pople JA (1972) Self-consistent molecular orbital methods. XII. Further extensions of gaussian-type basis sets for use in molecular orbital studies of organic molecules. *J. Chem. Phys.* 56(5):2257-2261.
32. Clark T, Chandrasekhar J, Spitznagel GW, & Schleyer PvR (1983) efficient diffuse function-augmented basis sets for anion calculations. III. The 3-21+G basis set for first-row elements, Li-F. *J. Comput. Chem.* 4(3):294--301.
33. Frisch MJ, Pople JA, & Binkley JS (1984) Self-consistent molecular orbital methods 25. Supplementary functions for Gaussian basis sets. *J. Chem. Phys.* 80(7):3265-3269.

34. Frisch MJ, *et al.* (2009) Gaussian 09 (Gaussian, Inc., Wallingford, CT, USA).
35. Spartan'14 (Wavefunction Inc., Irvine, CA).
36. Halgren TA (1996) Merck molecular force field. I. Basis, form, scope, parameterization, and performance of MMFF94. *J. Comp. Chem.* 17(5-6):490-519.
37. Halgren TA (1996) Merck molecular force field. II. MMFF94 van der Waals and electrostatic parameters for intermolecular interactions. *J. Comp. Chem.* 17(5-6):520-552.
38. Halgren TA (1996) Merck molecular force field. III. Molecular geometries and vibrational frequencies for MMFF94. *J. Comp. Chem.* 17(5-6):553-586.
39. Halgren TA & Nachbar RB (1996) Merck molecular force field. IV. conformational energies and geometries for MMFF94. *J. Comp. Chem.* 17(5-6):587-615.
40. Halgren TA (1996) Merck molecular force field. V. Extension of MMFF94 using experimental data, additional computational data, and empirical rules. *J. Comp. Chem.* 17(5-6):616-641.
41. Halgren TA (1999) MMFF VII. Characterization of MMFF94, MMFF94s, and other widely available force fields for conformational energies and for intermolecular-interaction energies and geometries. *J. Comp. Chem.* 20(7):730-748.
42. Kendall RA, Dunning, TH, & Harrison RJ (1992) Electron affinities of the first-row atoms revisited. Systematic basis sets and wave functions. *J. Chem. Phys.* 96(9):6796-6806.
43. Chai J-D & Head-Gordon M (2008) Long-range corrected hybrid density functionals with damped atom-atom dispersion corrections. *Phys. Chem. Chem. Phys.* 10(44):6615-6620.
44. Werner HJ, Knowles PJ, Knizia G, Manby FR, & Schtz M (2012) MOLPRO, version 2012.1, a package of ab initio programs.
45. Watts JD, Gauss J, & Bartlett RJ (1993) Coupled-cluster methods with noniterative triple excitations for restricted open-shell Hartree–Fock and other general single determinant reference functions. Energies and analytical gradients. *J. Chem. Phys.* 98(11):8718-8733.
46. Knizia G, Adler TB, & Werner HJ (2009) Simplified CCSD(T)-F12 methods: Theory and benchmarks. *J. Chem. Phys.* 130(5):20.
47. Adler TB, Knizia G, & Werner H-J (2007) A simple and efficient CCSD(T)-F12 approximation. *J. Chem. Phys.* 127(22):221106.
48. Werner H-J, Knizia G, & Manby FR (2011) Explicitly correlated coupled cluster methods with pair-specific geminals. *Mol. Phys.* 109(3):407-417.
49. Peterson KA, Adler TB, & Werner H-J (2008) Systematically convergent basis sets for explicitly correlated wavefunctions: The atoms H, He, B–Ne, and Al–Ar. *J. Chem. Phys.* 128(8):084102.
50. Eckart C (1930) The penetration of a potential barrier by electrons. *Phys. Rev.* 35(11):1303-1309.
51. Werner H-J, Knizia G, Adler Thomas B, & Marchetti O (2010) Benchmark studies for explicitly correlated perturbation and coupled cluster theories. in *Z. Phys. Chem.*, p 493.
52. Sha Y & Dibble TS (2016) Tunneling effect in 1,5 H-migration of a prototypical OOQOOH. *Chem. Phys. Lett.* 646:153-157.
53. Zhang F & Dibble TS (2011) Impact of tunneling on hydrogen-migration of the n-propylperoxy radical. *Phys. Chem. Chem. Phys.* 13(40):17969-17977.

54. Lin CY, Izgorodina EI, & Coote ML (2008) How accurate are approximate methods for evaluating partition functions for hindered internal rotations? *J. Phys. Chem. A* 112(9):1956-1964.
55. Orlando JJ & Tyndall GS (2012) Laboratory studies of organic peroxy radical chemistry: an overview with emphasis on recent issues of atmospheric significance. *Chem. Soc. Rev.* 41(19):6294-6317.
56. Jorand F, *et al.* (2003) Isomeric hexyl-ketohydroperoxides formed by reactions of hexoxy and hexylperoxy radicals in oxygen. *Int. J. Chem. Kinet.* 35(8):354-366.
57. Seinfeld JH & Pandis SN (1998) *Atmospheric chemistry and physics: from air pollution to climate change* (Wiley, New York).
58. Park J, Jongsma CG, Zhang R, & North SW (2004) OH/OD initiated oxidation of isoprene in the presence of O₂ and NO. *J. Phys. Chem. A* 108(48):10688-10697.
59. Vereecken L & Peeters J (2010) A structure-activity relationship for the rate coefficient of H-migration in substituted alkoxy radicals. *Phys. Chem. Chem. Phys.* 12(39):12608-12620.
60. Denisova TG & Denisov ET (2001) Kinetic parameters of alkyl, alkoxy, and peroxy radical isomerization. *Kinet. Catal.* 42(5):620-630.
61. Dibble TS (2004) Intramolecular hydrogen bonding and double h-atom transfer in peroxy and alkoxy radicals from isoprene. *J. Phys. Chem. A* 108(12):2199-2207.
62. Lim YB & Ziemann PJ (2009) Kinetics of the heterogeneous conversion of 1,4-hydroxycarbonyls to cyclic hemiacetals and dihydrofurans on organic aerosol particles. *Phys. Chem. Chem. Phys.* 11(36):8029-8039.
63. Aschmann SM, Arey J, & Atkinson R (2003) Kinetics and products of the gas-phase reaction of OH radicals with 5-Hydroxy-2-Pentanone at 296± 2 K. *J. Atmos. Chem.* 45(3):289-299.
64. Perrin O, Heiss A, Sahetchian K, Kerhoas L, & Einhorn J (1998) Determination of the isomerization rate constant HOCH₂CH₂CH₂CH(OO·)CH₃ → HOC·HCH₂CH₂CH(OOH)CH₃. Importance of intramolecular hydroperoxy isomerization in tropospheric chemistry. *Int. J. Chem. Kinet.* 30(12):875-887.
65. Jalan A, *et al.* (2013) New pathways for formation of acids and carbonyl products in low-temperature oxidation: the korcek decomposition of γ-ketohydroperoxides. *J. Am. Chem. Soc.* 135(30):11100-11114.
66. Jørgensen S, *et al.* (2016) Rapid hydrogen shift scrambling in hydroperoxy-substituted organic peroxy radicals. *J. Phys. Chem. A* 120(2):266-275.